Numerical Optimisation of Single- and Multi-Element Aerofoils Using Gradient-Based Methods

Xinying Liu[1][†], *David Anderegg*[1], *Anil Yildirim*[2], *Marcello Righi*[1] *and Leonardo Manfriani*[1]
[1]*Zurich University of Applied Sciences, Technikumstrasse 71, 8401 Winterthur, Switzerland*
[2]*University of Michigan, 1320 Beal Avenue Ann Arbor, MI 48109, USA*
[†]Corresponding author: xinying.liu@zhaw.ch

Abstract

High-fidelity flow solvers and gradient-based optimisers are two major components of efficient aerofoil shape optimisation tools for solving multi-objective industrial problems. In such cases, complex flow phenomena are involved and the number of design variables is large. The paper presents a review of aerodynamic aerofoil optimisation activities applying high-fidelity gradient-based methods at Zurich University of Applied Sciences (ZHAW). Two optimisation chains have been applied in research projects with industrial partners in the fields of wind energy and aeronautical engineering. To validate the numerical results, 2D drag measurements were carried out by measuring accurate velocity profiles downstream of the wind tunnel models using Constant Temperature Anemometry (CTA). The test campaigns were carried out in different subsonic wind tunnels in Switzerland. For the sake of publishing the applications without showing confidential information, this paper undertakes case studies of independent benchmarking scenarios that address similar objectives and constraints. The paper gives a brief description of both optimisation chains, outlines the optimisation setups of the selected case studies, and includes thorough analyses and discussions of the numerical and experimental data.

1. Introduction

The design of aerodynamic shapes for aerofoils holds great importance across industries including wind energy, motorsport, and aerospace. With the advancement of computational methods, the use of Computational Fluid Dynamics (CFD) tools for aerofoil optimisation has become crucial in recent years. Aerofoil optimisation problems have been shown to be unimodal and well-disposed to solution by gradient-based optimisers.[3] This paper provides an overview of industrial applications conducted at Zurich University of Applied Sciences (ZHAW). It introduces two optimisation tools based on gradient-based methods.

One of the optimisation chains applied relies on the MACH framework made available as open-source software by the MDO Lab at the University of Michigan. Its components may also be exploited in conjunction with OpenMDAO,[7] an open-source general-purpose optimisation framework. Part of the MACH framework is ADflow, an open-source Reynolds-Averaged-Navier-Stokes (RANS) CFD solver using structured multiblock and overset grids. It relies on the discrete adjoint method[5] to assess the sensitivities of the design variables. The aerofoil geometry is parametrised using Free-Form-Deformation (FFD) and additional design variables to account for the kinematics of multi-element aerofoils. It is worthwhile noting that the chosen methodologies may be easily extended to Multi-Disciplinary Optimisation (MDO) using OpenMDAO, as they are particularly useful for efficiently computing derivatives across computational models. The turbulence model used in the first optimisation process was Spalart-Allmaras[15] (SA). To effectively optimise multi-element aerofoils, grid deformation and re-meshing policies were modified.

The second optimization process was driven by the commercial finite-volume CFD solver Ansys Fluent[1] with structured grids. The discrete adjoint approach was adopted to compute the derivatives of an observation of the flow surrounding the aerofoils, providing shape-sensitivity data. The problem of shape parametrisation of an entire aerofoil is therefore reduced to a problem of parametrising the changes of the aerofoil shape. In the mesh morphing process, the designated deformation regions used structured grids and were manipulated via displacements applied to a set of control points. The user-defined motions that result in the displacements of the control points (each involving a parameter value and other directional settings) were then applied to the grid as a smooth deformation by using the tensor product of B-splines and Bernstein polynomials. A generalized $k - \omega$ two-equation (GEKO) turbulence model[9] was used in this optimisation process.

X. LIU, D. ANDEREGG, A. YILDIRIM, M. RIGHI, L. MANFRIANI

To validate the 2D numerical results, test campaigns were conducted in different subsonic wind tunnels in Switzerland. The first was the large subsonic wind tunnel of the Federal Institute Technology in Zurich (ETHZ), and the second was the Automotive Wind Tunnel Emmen (AWTE) at RUAG. 2D drag measurements were carried out by measuring accurate velocity profiles downstream of the wind tunnel model using Constant Temperature Anemometry (CTA).

The work carried out is confidential. For the sake of publishing, three independent benchmark cases with similar optimisation objectives and constraints are discussed in this paper. The goal of the present paper is to demonstrate the versatility and usefulness of the two high-fidelity gradient-based methods used at ZHAW for aerofoil design. While most of the aforementioned tools were developed and implemented previously, this paper is more related to application and analysis. It addresses common concerns of gradient-based optimisation approaches and provides practical strategies to the aerofoil designers in industry.

The present paper is structured as follows. We describe briefly the numerical optimization methods and wind tunnel setup in Section 2. Section 3 outlines the optimisation goal and setup of each case study. Section 4 presents the results and is followed by the conclusion in Section 5.

2. Methodology and Tools

2.1 Numerical Methods
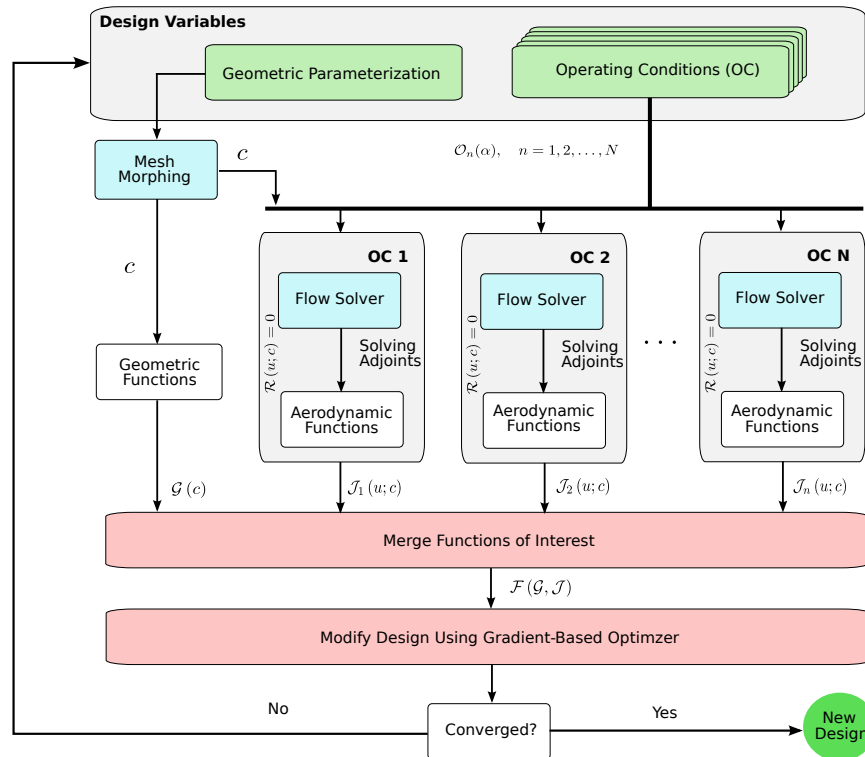
2.1.1   Gradient-Based Optimisation

Figure 1: Workflow of aerofoil optimisation using the adjoint method

The present subsection gives an overview of the general workflow of both optimisation chains. The following subsections then explain the slight differences in their implementation. Figure 1 illustrates the workflow of a gradient-based optimisation. It shows the adjoint method integrated in the finite-volume RANS Solvers used in this study.

Shape optimisation involves modifying a design shape in order to improve specific quantities of interest in a fluid system, such as aerodynamic performance, while maintaining the specified geometric functions $\mathcal{G}$ of the engineering problems. The input data governing the shape design are known as Design Variable (DV), and the quantities of interest

are referred to as functions of interest, denoted as $\mathcal{J}$. Given the extensive set of DVs and flow solution from CFD solver, a fluid system can generate a vast array of derivative data. The matrix of derivatives represents the relationship between the DVs and the functions of interest. In practical applications, the optimisation process adopts the adjoint method to efficiently calculate the derivatives of engineering functions of interest with respect to a large number of DVs. DVs are categorised in two groups: geometric parameters and operating conditions (OC, denoted as O). The latter specify environmental variables of the flow simulations, such as Angle of Attack (AoA), Re-number or/and parameters for turbulence models. ADflow and Ansys Fluent parameterise the aerofoil and morph the existing mesh using the FFD approach. As output of the mesh morphing procedure, a deformation vector c on the cells forms the geometric functions $\mathcal{G}(c)$, which are utilized as constraints in the optimisation process. The deformed grid is used for the flow computation at each OC. The flow variables u, like pressure and velocity, are solved by satisfying conservation of mass and momentum, read as

$$\mathcal{R}(u; c) = 0 \tag{1}$$

The adjoint solver determines sensitivities of the aerodynamic functions $\mathcal{J}$ with respect to the geometry deformation c and flow variables at the specific DP

$$\delta \mathcal{J}_n = \frac{\partial \mathcal{J}_n}{\partial u} \delta u + \left. \frac{\partial \mathcal{J}_n}{\partial c} \right|_u \delta c \tag{2}$$

where n denotes the number of DP and $|_u$ denotes that the flow solution is held constant while the derivative is taken.

The subsequent step involves gathering sensitivity data for the aerodynamic functions at each point to determine the optimal design modification with respect to the geometric functions. The described process is repeated until convergence is achieved, resulting in a new design.

2.1.2 Pre-Processing

Grid generation and topology. We used structured O-grids with a farfield boundary condition for the flow computation. The generation of the multi-block overset grids for ADflow was accomplished using the pyHyp library*. The adjoint solver in the Ansys version used does not support multi-block overset grids. Therefore, single-block grids were generated using the commercial grid-generation tool Pointwise. As part of a grid-independence study, the new designs obtained were tested using overset-multiblock O-grids in Ansys Fluent. The grid parameters are listed in Table 1.

Parameter	Single-Element Aerofoil	Multi-Element Aerofoil
Chord length	1	
Farfield distance	> 300	
$Y+$ dimensionless wall distance	< 0.5	
Number of Cells	$\approx 50\,000$	$\approx 150\,000$

Table 1: Grid parameters.

Geometric parameterisation and morphing. Both ADflow and Ansys Fluent adopt the FFD method to parameterize the aerofoil geometry. They differ slightly in implementation. For a 2D case, $N_w \times N_v$ control points $P_{i,j}$, where $i = 0, \ldots, N_w - 1$ and $j = 0, \ldots, N_v - 1$, are distributed in a control volume based on a (w, v) coordinate system. The motions of the cells in the calculation domain are determined by the movements of the control point motions, using B-splines. The parametric equation of B-splines can be written as

$$S(w, v) = \sum_{i=0}^{N_w - 1} \sum_{j=0}^{N_v - 1} \mathcal{N}_{i,p_w}(w) \mathcal{N}_{j,p_v}(v) P_{i,j} \tag{3}$$

with B-splines of p degree defined as follows

$$\mathcal{N}_{i,0}(w) = \begin{cases} 1 & \text{if } t_i \leq u < t_{i+1} \\ 0 & \text{otherwise} \end{cases}$$
$$\mathcal{N}_{i,p}(w) = \frac{w - t_i}{t_{i+p} - t_i} \mathcal{N}_{i,p-1} + \frac{t_{i+p+1} - w}{t_{i+p+1} - t_{i+1}} \mathcal{N}_{i+1,p-1}, \tag{4}$$

where w is the parametric location with respect to knots t_i. The derivative of a point in the 2D domain with respect to a control point $P_{i,j}$ is determined by differentiating Equation 3. The change of the node can be calculated by adding

---

*https://github.com/mdolab/pyhyp

the displacements with respect to all the control points associated with the B-splines. However, the displacements of the surface nodes are not always of the same order as that of grid off-wall spacing. Therefore, a part of the volume grid has to be modified to prevent negative volume cells. Ansys Fluent employs the aforementioned B-spline controls for fine-scale motion, while utilizing Bernstein polynomials to control large-scale deformation. For the mesh warping with ADflow, we used the IDWarp package[†] based on an inverse distance weighting approach.[14]

2.1.3 Flow Solver and Adjoint Method

Flow Solver. ADflow and Ansys Fluent use a finite-volume scheme to solve the RANS equations. We used the approximate Newton-Krylov solver and the SA turbulence model to solve those equations in ADflow. This combination resulted in a very short "time-to-solution".[12] In Ansys Fluent, the adjoint solver is only compatible with two-equation turbulence models. We used a new turbulence model family called GEKO. In the present study, the GEKO model was set the Shear Stress Transport[8] (SST) turbulence model[9] and the turbulence model parameters were fixed during the optimisation process.

Adjoint Method. Following Equation 2, the summation of sensitivities data of aerodynamic functions $d\mathcal{J}/dc$ can be expressed as

$$\frac{d\mathcal{J}}{dc} = \frac{\partial \mathcal{J}}{\partial c} + \tilde{u}^T \frac{\partial \mathcal{R}}{\partial c} \tag{5}$$

The adjoint problem is nothing other than solving the following equation

$$\left[\frac{\partial \mathcal{R}}{\partial u}\right]^T \tilde{u} = -\left[\frac{\partial \mathcal{J}}{\partial u}\right]^T \tag{6}$$

Both adjoint solvers follow the discrete adjoint approach consisting of two general steps: (1) discretize the flow solver first, then (2) derive the exact discretized adjoint equation for the discretized flow solver system. The adjoint solver methodology is based on an iterative procedure: calculating adjoint residual $\tilde{\mathcal{R}}$, determining correction to adjoint equations using corrected adjoint vector and updating adjoint equations.

2.1.4 Boundary Conditions

We defined the outer boundary of the O-grids as "pressure farfield" with a eference pressure of $P_{ref} = 10^5$ Pa, a temperature of $T_{ref} = 288$ K and a Mach number of $Ma = 0.15$. The Reynolds-number Re varied between $10^5 - 5 \times 10^6$. It was adapted by changing the fluid's viscosity. To study surface contamination, we applied surface roughness k_s using Equivalent Sand-Grain Roughness[13] on the aerofoil surface with a "no-slip wall" boundary condition.

2.1.5 Coupling Framework and Optimiser

For the ADflow optimisation chain, the optimiser used is called SNOPT[‡]. It is based on the Sequential Quadratic Programming (SQP) approach. All the optimisation processes associated with Ansys Fluent were carried out in Ansys Workbench. It is a multi-physics platform managing data across all Ansys products. The grids of each baseline-aerofoil was generated using Pointwise and imported in Ansys Fluent. Ansys Fluent includes a gradient-based optimiser.

2.2 Wind Tunnel Testing

To support the numerical optimisation, various wind tunnel campaigns were carried out in wind tunnels in Switzerland. As example, Figure 2 (a) illustrates the installation of sing-element aerofoil in the large wind tunnel of ETHZ. A constant section wing was built for the optimised aerofoils. The wing was installed vertically, constrained on both ends and spanned from the bottom to the ceiling of the test section. Forces and measurements were measured by the wind tunnel balance connected to the floor attachment. In addition, drag measurements relied on the accurate velocity profile downstream of the model using a CTA system. The AWTE wind tunnel at RUAG was used for testing multi-element aerofoils. As shown in Figure 2 (b), the wing was placed vertically in the open test section. For the 2D measurements, only the forces and moments on the middle section were evaluated. It can be seen that the traverse for the CTA measurements was located downstream the wind tunnel model. All models were CNC machined out of various polymers. Soiled conditions were addressed by varying the surface roughness by applying sand paper strips of different grain size. Referring to our previous studies and experimental work[6] from other research groups, 150-grit and 220-grit were chosen to replicate the effects of erosion as well as other contamination types like insects and oil.

[†] https://github.com/mdolab/idwarp

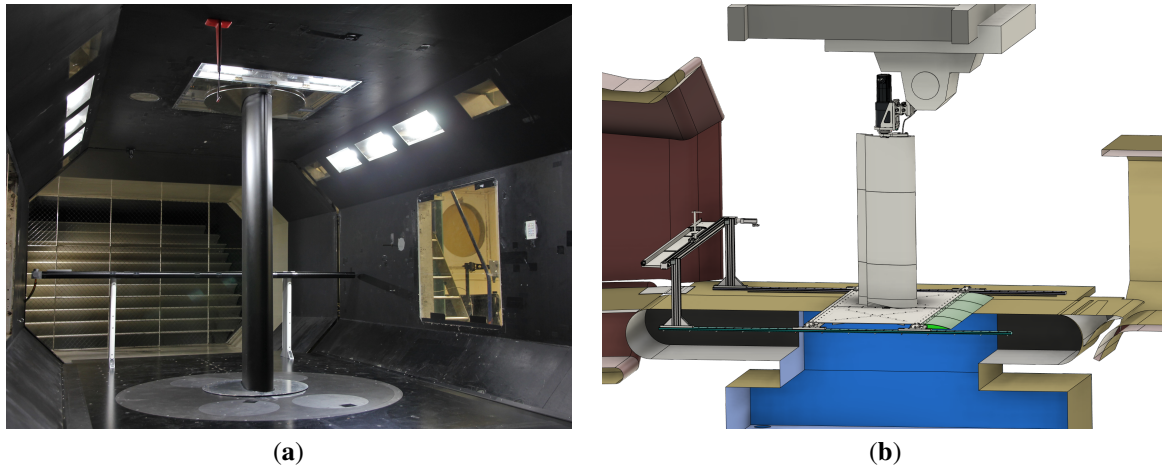[‡] https://www.sbsi-sol-optimize.com/asp/sol_snopt.htm

(a) (b)

Figure 2: Wind tunnel installation: (a) single-element aerofoil test in the subsonic wind tunnel at ETHZ; (b) multi-element aerofoil test in the AWTE open wind tunnel at RUAG.

3. Case Studies

3.1 Single-Element Aerofoil Optimization

3.1.1 Optimisation Goals and Constraints

The first case deals with a single-element aerofoil optimisation for a vertical axis wind turbine. This optimisation was performed using ADflow. A series of optimisation exercises was carried out on a group of aerofoils characterized by its thickness. It varies between 18% and 50% of chord length.[12] In the present, independent case study, the objectives, constraints and operating conditions are summarised as follows:

Geometric Constraints. To guarantee manufacturability and ease of handing, it is essential to maintain a minimum thickness $(t/c)_{min}$ at the trailing edge. Because the aerofoil has to work the same for positive and negative angles of attack, it symmetrically constrained. For structural reasons, the aerofoil thickness should be at least 27% of chord length. The Centre of Pressure (CoP) must be behind the rotation point of the blade. To minimize angular momentum, the rotation point should lie on the center of gravity. This means in practice, the CoP of the airfoil needs to be pushed back as far as possible without decreasing aerodynamic efficiency.

Performance Objectives. The lift-over-drag value was defined as the objective of the optimisation. It was expected that the aerodynamic efficiency of the optimised aereofoil meets at least the level of a NACA 4-digit aerofoil with comparable thickness (while having an improved CoP).

Operating Conditions. Based on the outcomes of the previous studies, surface contamination plays an important role for thick airfoils. This means, the performance of the aerofoil under soiled conditions had to be taken into account as well. The considered Reynolds number ranges from Re $= 1 \times 10^6$ to 5×10^6.
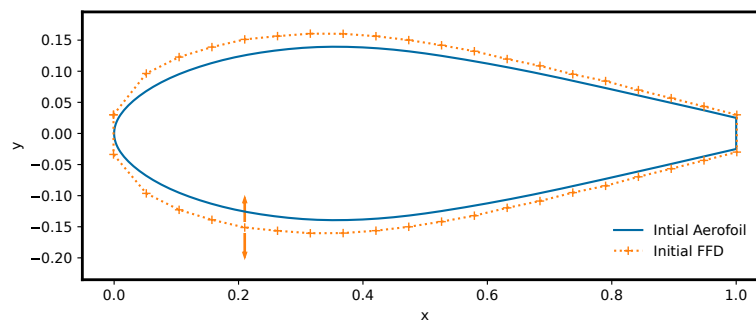
3.1.2 Optimisation Approach

Figure 3: The initial airfoil and its FFD box for the single-element optimisation using ADflow.

X. LIU, D. ANDEREGG, A. YILDIRIM, M. RIGHI, L. MANFRIANI

Geometric Parametrisation. We used the FFD approach to create control points around an initial aerofoil with the target aerofoil maximal thickness. Figure 3 presents the initial aerofoil in blue and the FFD box in orange, on which 40 control points are symmetrically positioned. The displacement of each control point occurs in vertical axis.

Design Points. As listed in Table 2, we defined eight design points, taking into account the aforementioned optimisation objectives. In addition, we aimed to decrease the drag coefficient C_d at AoA = 0° for smoother surface.

Constraints. The geometric and performance constrains are listed in Table 3.

Objective. All functions of interest are merged with weighting factors w_i, where $i = 1, 2, 3, 4$. The total objective function $\mathcal{F}$ can be written in Equation 2, where the overlines denote the expectation values of the optimisation and x_{cp} denotes the CoP position.

Design Point	AoA	Comment
0	9°	Increase $(L/D)_{max}$
1-5	13° - 17°	Control stall behaviour
6	0°	Decrease C_d for a smoother surface
7	10°	Soiled condition

Table 2: Constraints for single-element aerofoil optimisation using ADflow.

Variable	Value	Comment
$(t/c)_{min}$	$\geq t_{min}\%$	Set minimal trailing edge thickness
$(t/c)_{max}$	$\geq 27\%$	Aerofoil thickness constraint
$|dC_l/\,d\alpha|_{max}$	≤ 0.2	Prevent abrupt stall behaviour

Table 3: Design points for single-element aerofoil optimisation using ADflow.

$$\mathcal{F} = \left(\frac{\overline{C_l/C_d}}{Cl/C_d}\right)_{clean} \cdot w_0 + \left(\frac{\overline{C_l/C_d}}{Cl/C_d}\right)_{rough} \cdot w_1 + \frac{\overline{x_{cp}}}{x_{cp}} \cdot w_2 + \frac{C_d}{\overline{\overline{C_d}}}\bigg|_{AoA=0°} \cdot w_3 \tag{7}$$

3.2 Multi-Element Aerofoil Optimization I

3.2.1 Case Description

For the second case, we focused on the airborne wind energy sector. This approach involves harnessing energy by flying a tethered, unmanned aerial vehicle (UAV). It exploits the fast winds at higher altitudes compared to conventional wind energy turbines. The aim of the aerofoil optimisation is to improve the kite performance of said UAV. Its definition[4] is written as

$$P_{kite} = \frac{C_L^3}{C_D^2} \tag{8}$$

where C_L and C_D denote the 3D lift and drag coefficient of the tethered UAV. In the current exercise, C_L is approximated by the 2D lift coefficient C_l. The 3D drag coefficient C_D can be written as

$$C_D = C_d + C_{d_i} + C_{D_{tether}} + C_{D_{other}} \tag{9}$$

where the induced drag C_{d_i} can be calculated with a constant wing efficiency factor and aspect ratio. The drag coefficients of the tether with a constant length and other 3D features are assumed to be constant. We conducted the optimisation using Ansys Fluent,with the following requirements:

Geometric Constraints. In order to adhere to the structural requirements, the area and thickness of baseline aerofoil should be defined as the lower limit for the new design. This applies to the aerofoil thickness as well.

Performance Objectives. The goal is to improve the kite performance. Also, the aerofoil should be robust against disturbances and represent a mild stall behaviour.

Operation Conditions. A relative large operating range of ±5° flap deflection should be achieved without much reduction of kite-performance. The Reynolds number is Re = 5×10^6. Additionally, it would be desirable if the aerofoil also had good performance at lower Reynolds numbers.

3.2.2 Optimisation Approach

In the iterative design process, we combined Ansys Fluent gradient-based optimisation tool with other shape design methods. In order to smooth the aerofoil shape to improve its robustness, we applied the conventional inverse method with desired velocity distributions in potential flow using panel code. It was treated as fine-tuning process based on the outputs from the gradient-based optimisation. In the previous studies, we found that it was unrealistic to satisfy all the expectations on the functions of interest at all design points. Practically, it would be more effective to prioritize the design points of greatest interest initially. Furthermore, the performance of the main section has a significant impact on the overall performance of the multi-element aerofoil. At the main design point $Re = 5 \times 10^6$, we used the gradient-based optimiser for the base element of the aerofoil, while fixing the flap position. Subsequently, we optimised the flap position using an add-on, goal-driven optimisation tool called Ansys DesignXplorer. We repeated the procedure with weighted target expectations at other design points.
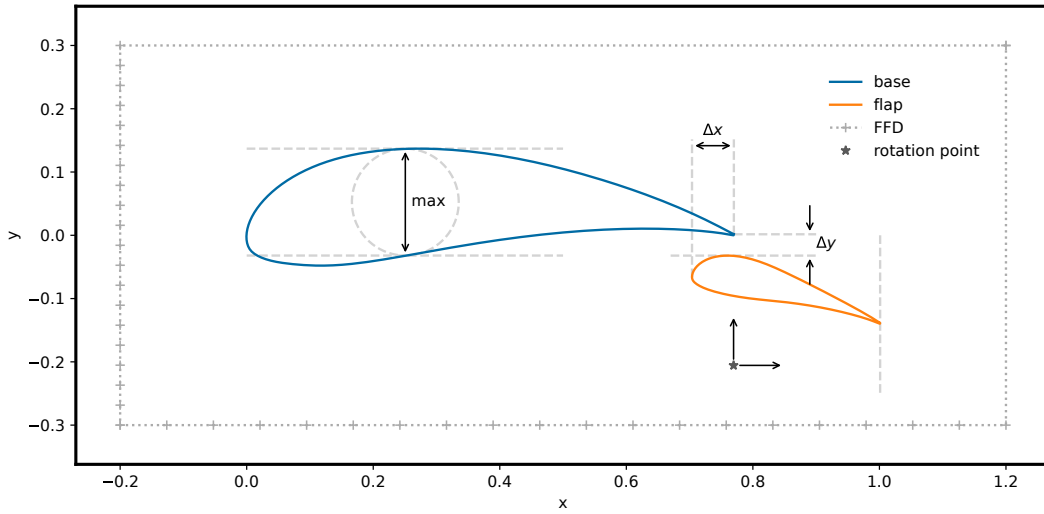

Figure 4: Geometric parametrisation for the multi-element optimisation using Ansys fluent.

Geometric Parametrisation. Figure 4 shows the geometric parametrisation. The FFD box with uniform distribution of control points in the x, y directions define the region of space where a design change is applied. The grey dashed line in the FFD box are defined as global bounds with respect to the geometric constraints. The circle controls the aerofoil thickness and can be translated in x direction. In addition, the rotation point of the flap and flap deflection are defined as design variables for a goal-driven optimisation. To ensure satisfactory grid quality in the gap between the two-element aerofoils, a minimum distance Δy between the trailing edge and upper side of the flap is set. Δx denotes the horizontal overlap of the two elements.

Optimisation Setup. The optimisation can be generally summarized in three rounds.The outcome of the optimisation at $Re = 5 \times 10^6$ was further tested and subsequently slightly modified at $Re = 1 \times 10^6$. The aim was to cover a relatively broad operational range. To conduct a flap deflection study, several flap configurations are defined in Table 4. The specific details of each round are summarised in Table 5. Each round produced a design with representative aerodynamic characteristics.

Name	Description
clean	Basic point for the traction phase
clean_up	$C_{l_{clean}} - C_{l_{cleanUp}} = 0.5$
clean_down	$C_{l_{clean}} - C_{l_{cleanDown}} = -0.5$
cl0	Lower limit of lift for efficient retraction phase

Table 4: Design points for multi-element aerofoil optimisation using Ansys fluent.

X. LIU, D. ANDEREGG, A. YILDIRIM, M. RIGHI, L. MANFRIANI

Round	Description	Optimisation Method		
		Gradient-Based	Design of Experiment	Inverse Method
A	Step 1: increase P_{kite} and decrease C_d at AoA= 10° and 15°	×		
	Step 2: increase P_{kite} and decrease C_d at AoA= 12° and increase C_l at AoA= 13°	×	×	
	Step 3: Smooth velocity distributions on main section at AoA= $10-13°$			×
B	Step 1: hold P_{kite} with ±10% tolerance and decrease C_d at AoA= 8° and 13°	×	×	
	Step 2: increase P_{kite} and C_l at AoA= 13°	×	×	
	Step 3: hold C_d with ±5% tolerance and increase C_l at AoA= 13 and 16°	×	×	
C	Step 1: Smooth velocity distributions at AoA= $13-16°$			×

Table 5: Summary of the optimisation process.

3.3 Multi-Element Aerofoil Optimization II

3.3.1 Case Description

Porta Ko et al.,[10] optimised a two-element aerofoil for a fixed-wing airborne energy system. Their setup was somewhat similar to what we did and this is why we chose it as a test case. The goal is to optimise the aerofoil for a fixed-wing airborne energy system using ADflow. This puts specific demands on its performance and geometry which[10] quantifies as follows:

Geometric Constraint. Min thickness of the aerofoil is 20 % of its chord.

Performance Objectives. Maximum P_{kite}[§] at design lift coefficient (**cl_des**). Maximum P_{kite} at $C_l = 70\%$ of **cl_des**. This point is called **cl_2**. Sufficient stall margin. This means $C_l @ C_{l_{max}} = 0.8 * C_l @ C_{l_{des}}$. Low $C_{l_{min}}$ (**cl0**) to swiftly retract the tether.

Operation Conditions. The aerofoil should operate at a Reynolds number Re = 3×10^6.

To clarify the nomenclature: The main section of the aerofoil is called *base* and the trailing edge device is called *flap*.
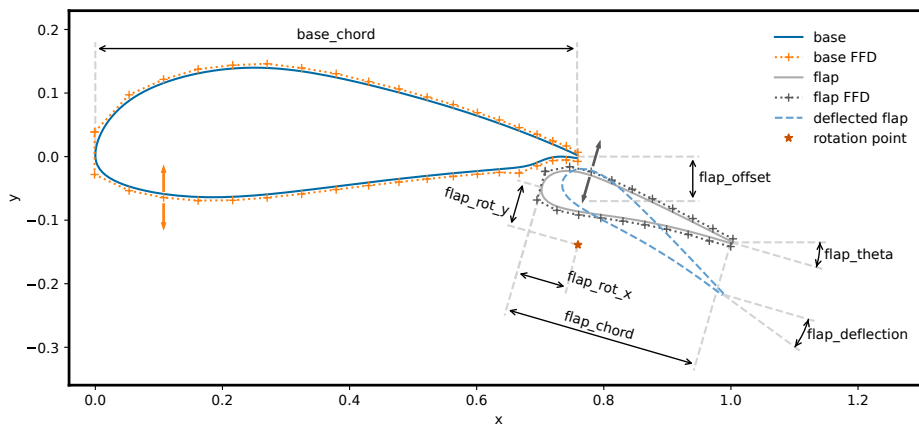
3.3.2 Optimisation Approach

Figure 5: Geometric parametrisation for the multi-element aerofoil optimisation using ADflow.

[§]In accordance with the setup in Porta Ko et al.,[10] we neglected the 3D drag and used the simplified definition $P_{kite} = \frac{C_l^{1.5}}{C_d}$

Geometric Parametrisation. The design variables for the geometric parametrisation fall into two categories: *local* and *global*. The *local* variables are basic FFD boxes around each element. The points are allowed to move perpendicularly to the chord. This can be seen in Figure 5. The *global* variables define the relationship of both elements to each other, for instance the *vertical offset* of the flap. The leading edge of the base element is located at $x = 0, y = 0$ and the trailing edge lies on the $y = 0$ line. This line is also the reference for the angle of attack. The flap angle is defined by two seperate angles: *flap_theta* and *flap_deflection*. The first one is the basic angle of the flap when it is not deflected. In that state, the trailing edge of the flap lies on the $x = 1$ line. The *flap_deflection* defines how much the flap is rotated around the rotation point when being deflected. Apart from **alpha** and **flap_deflection**, all design variables are the same for all design points.

Design Points. Derived from the demands mentioned in section 3.3, Table 6 lists all design points.

Constraints. Table 7 lists all constraints that were derived from section 3.3.

Objective. Porta Ko et al.[10] used a genetic algorithm to optimise the aerofoil employing a multi-objective. In gradient based optimisation, this is not possible. Thus the following formula and weights were used to assemble one single objective value. The weights and expected values are derived from experience and experimenting. Drag at **cl0** is minimized to make sure the flow remains attached.

Name	Comment
cl_des	This is the primary desgin point. Here, P_{kite} will be maximised. The flap is not be deflected ; only the default flap angle (**flap_theta**) may change.
cl_max	Make sure we have a sufficient stall margin. The geometry is exactly the same as in **cl_des**. Only AoA is allowed to change.
cl_2	This is the secondary design point. Also P_{kite} will increase as much as possible. The optimiser is allowed to deflect the flap (**flap_deflection**) and the Angle of Attack.
cl0	This design point makes sure a sufficient low C_l is achievable. The optimiser is allowed to the deflect the flap and change the AoA.

Table 6: Design points for multi-element aerofoil optimisation using ADflow.

Name	*Value*	Comment
tc_max	≥ 0.2	The thickness to chord ratio.
cl_max_des_diff	$C_l@C_{l_{max}} = C_l@C_{l_{des}} \cdot 0.8$	C_l at **Cl_des** should be 80% of that at **Cl_max**.
cl_des_2_diff	$C_l@C_{l_2} = C_l@C_{l_{des}} \cdot 0.7$	C_l at **Cl_2** should be 70% of that at **Cl_des**.
cl_min	$C_l@C_{l_{min}} \leq -0.4$	The lowest C_l (where the flow is still attached) should be less than -0.4

Table 7: Constraints for multi-element aerofoil optimisation using ADflow.

$$\mathcal{F} = (150/P_{kite}@C_{l_{des}} \cdot 1 + 150/P_{kite}@C_{l_2} \cdot 1 + C_d@C_{l_{min}}/0.015 \cdot 0.5)/2.5 \tag{10}$$

4. Results and Discussion

4.1 Single-Element Aerofoil Optimization

The optimised aerofoil was tested numerically and experimentally with and without consideration of wall roughness. There is no direct correlation between the mathematical model used to simulate a contained surface. But we found in the previous studies that the roughness of a 220-grit sand paper is close to an equivalent sand grain roughness of $k_s = 10^{-4}\ m$. Figure 6 compares the aerodynamic coefficients of the new design at $Re = 10^6$ with predicted CFD values. The C_l and C_m slopes match very well for the clean and rough configurations. The C_d curves also show a very similar behaviour. The differences observed at low AoAs are mainly due to strong signal oscillations in the wind tunnel.

Further, we evaluated the aerodynamic performance of the new design at various Reynolds-numbers and compared it with existing experimental data[2] of a NACA 0025 aerofoil. Figure 7 presents the aerodynamic coefficients of NACA 0025 in clean conditions and with a deflected flap of $15°$ at $Re = 2.9 \times 10^5$. The numerical results of the new design are at $Re = 1 - 5 \times 10^6$. The optimised new design shows a significantly better lift-to-drag ratio than the original NACA 0025. The new design also presents a mild stall behaviour, especially at low Reynolds-numbers. Here, NACA

4-digit aerofoils with such high thicknesses suffer from high adverse pressure gradients on the suction side which leads to an abrupt stall after reaching the maximum lift.
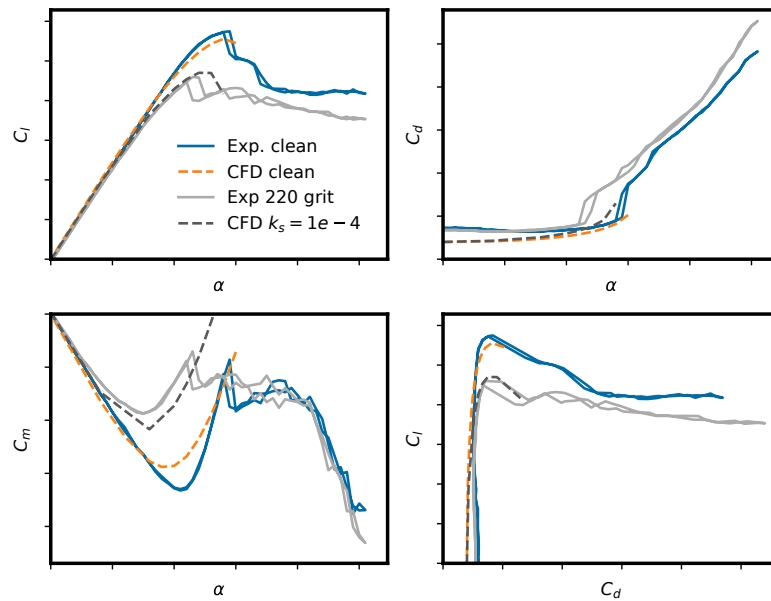

Figure 6: Experimental and CFD aerodynamic coefficients for the new single-element aerofoil at $Re = 10^6$.
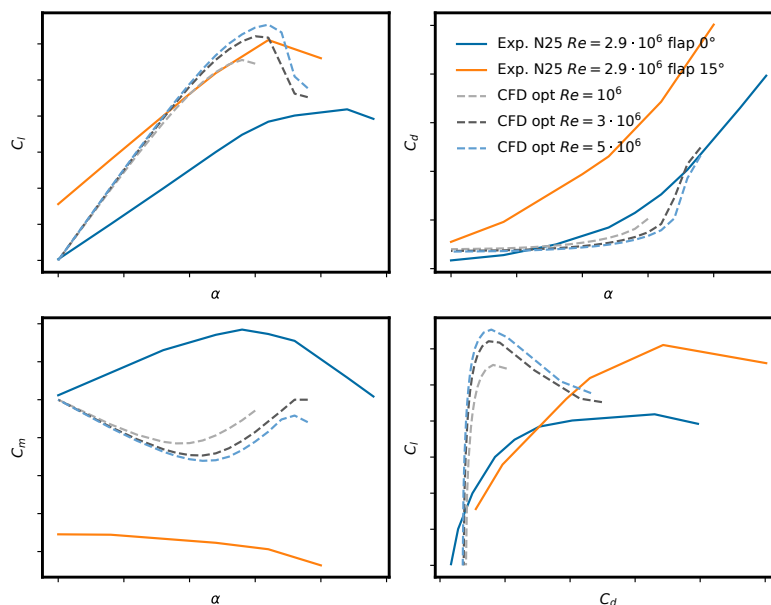

Figure 7: Comparison of aerodynamic coefficients between the new single-element aerofoil and NACA0025.

During the optimisation process, we noticed that optimiser quickly turnes to systematically increasing the aerofoil trailing edge height or to minimising the thickness near the trailing edge abruptly. It does this to minimize the adverse pressure gradients on one hand, and simultaneously results in a forced separation on the other hand. Based on the gained experience in the wind tunnel, it became clear that roughness has addition impacts on the boundary layer growth. Due to that, we traded a small amount of efficiency for robustness. It is worth mentioning that a quasi symmetrical aerofoil DU12W262[11] with a profile thickness of 26% chord length could meet all the design requirements in the present case study. This aerofoil was optimised by TU Delft specifically for VAWT application. However, the remarkable performance penalty under rough surface condition was considered a main drawback. This sensitive effect on roughness leading to a dramatic increase in drag was confirmed by experimental data in their paper. This agrees

with our numerical results (not shown) obtained in a preliminary study.

As mentioned previously in Section 3.1.1, one of the objective is to have a CoP as far back as possible. As the CoP of the present new design is located between 25%-30% of the chord lenght, we added an (optimised) offset cavity on the flatback trailing edge. This did not disturb the existing aerofoil performance and achieved to push the Cop backwards by additional 5%. The offset cavity optimisation was carried out separately and was less time-consuming than the shape optimisation of the whole aerofoil.

4.2 Multi-Element Aerofoil Optimization I
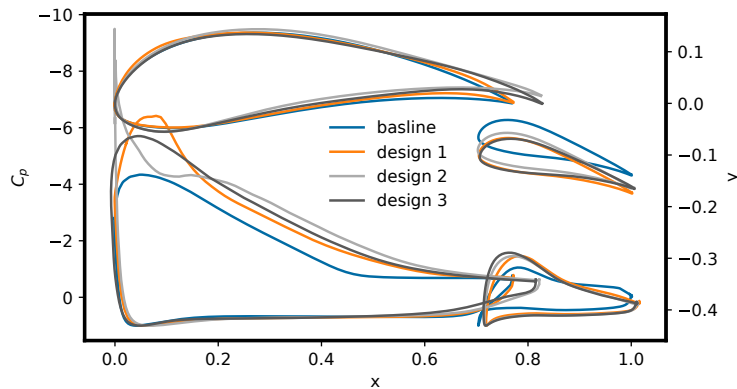
Figure 8: Baseline and new design shapes and their pressure distributions at AoA = 13° and Re = 5×10^6 (multi-element Ansys).
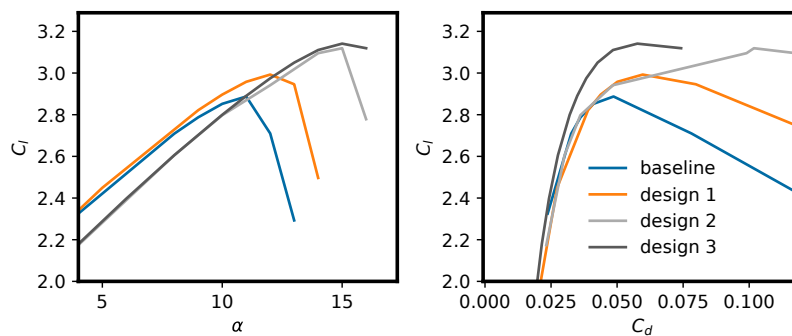

Figure 9: Aerodynamic coefficients of baseline and new design shapes at Re= 5×10^6 (multi-element Ansys).

We summarised the various design iterations in three rounds. Each round reflects a significant stage of the evolution. Figure 8 presents the baseline aerofoil and the three new designs and their pressure distributions at AOA = 13° and Re $= 5 \times 10^6$. The lift and drag coefficients of the four aerofoils are presented in Figure 9

With the geometric constraints on the aerofoil's area and maximal thickness, the optimiser turns to form a drop nose and a plain flap. Consequently, the separated flow downstream $\approx$ 50% chord length (see C_p distribution of baseline aerofoil in 9) became attached. A subsequent chamber increase leads to the extension of the stall AoA, respectively a mild stall behaviour. The second round of optimisation was carried out more aggressively with the intention to increase the pressure peak on the suction side. The strategy increased the maximal lift at the expense of an abrupt chamber change downstream the maximum thickness position. This could harm the robustness of the aerofoil. Due to the results obtained from round 1 and round 2, we focused on shaping the aerofoil using the conventional inverse method associated with potential flow theory in round 3. This significantly improved performance shown in Figure 9 confirms the high efficiency of this method for fine-tuning.

To check the aerofoil performance under other operating configurations, we analyse the data in lower Reynolds numbers and with different flaps. Figure 10 presents aerodynamic coefficients measured and calculated at Re= $1 - 2 \times 10^6$. The analysis of Figure 10 shows very similar lift and drag slopes and a quantitatively compatible maximum lift coefficient. The discrepancies in stall behaviour might be due to that the transition to turbulence effects were not

included in the simulations. A transitional turbulence model could show a better match. It can be seen that we traded the stall behaviour at lower Reynolds numbers. We are confident that the stall behaviour can be improved by adjusting the weighting factors for different Reynolds numbers.

Figure 11 presents the results of a flap deflection study. All the numerical results at Re $= 5 \times 10^6$ are plotted as a function of AoA and Flap deflection. The green markers indicate operating points. The chart background is coloured using C_l (left) and P_{kite} (right) values. The analysis shows that the aerofoil maintains good kite performance ranging from 110 - 150 in the area of steering (**clean_down** to **clean_up**) with 20° flap deflection. However, we do see the optimisation potential of the current design at clean_up. This could be achieved with further Design of Experiments (DoE) for the flap positions using goal-driven optimisation.
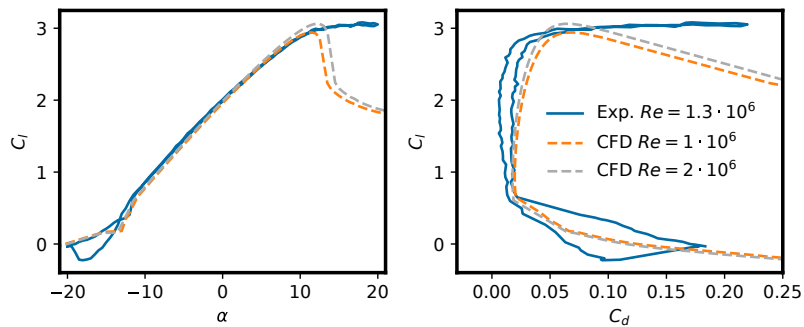

Figure 10: Numerical and experimental aerodynamic coefficients of new design at Re $= 1 - 2 \times 10^6$ (multi-element Ansys).
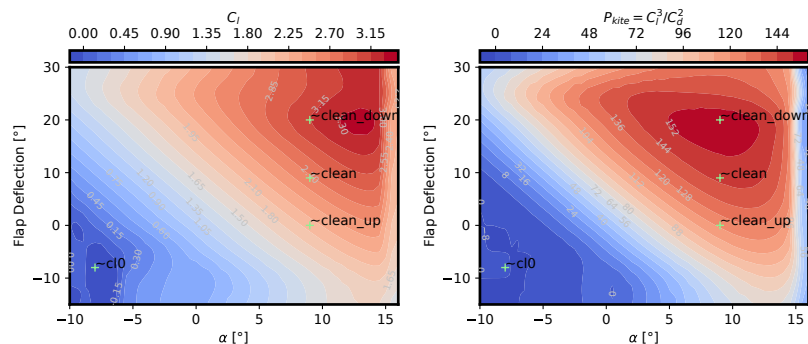

Figure 11: Flap deflection study of new design at Re $= 5 \times 10^6$ (multi-element Ansys).

4.3 Multi-Element Aerofoil Optimization II
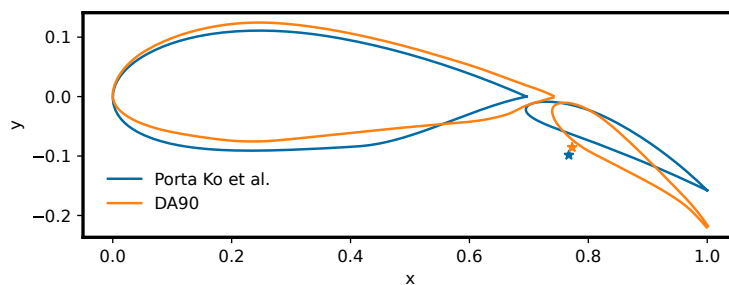
4.3.1 Aerofoil geometry

Figure 12: Comparision of Porta Ko et al.[10] and DA90 aerofoils.

The resulting airfoil is called *DA90*. Figure 12 shows it together with the reference airfoil from Porta Ko et al.[10] *DA90* has a longer chord and a steeper flap angle. This indicates a more aggressive approach and thus a higher lift coefficient. Also the rotation point is closer to the flap. It has to be noted that the optimiser would have liked to pull it up even further. Due to numerical problems, this was prevented by bounding the design variables. When looking closely at the trailing edge of the base element of *DA90*, it can be seen that additional FFD-points would be needed to achieve a truly smooth surface. Both problems could have been addressed if more time was available.
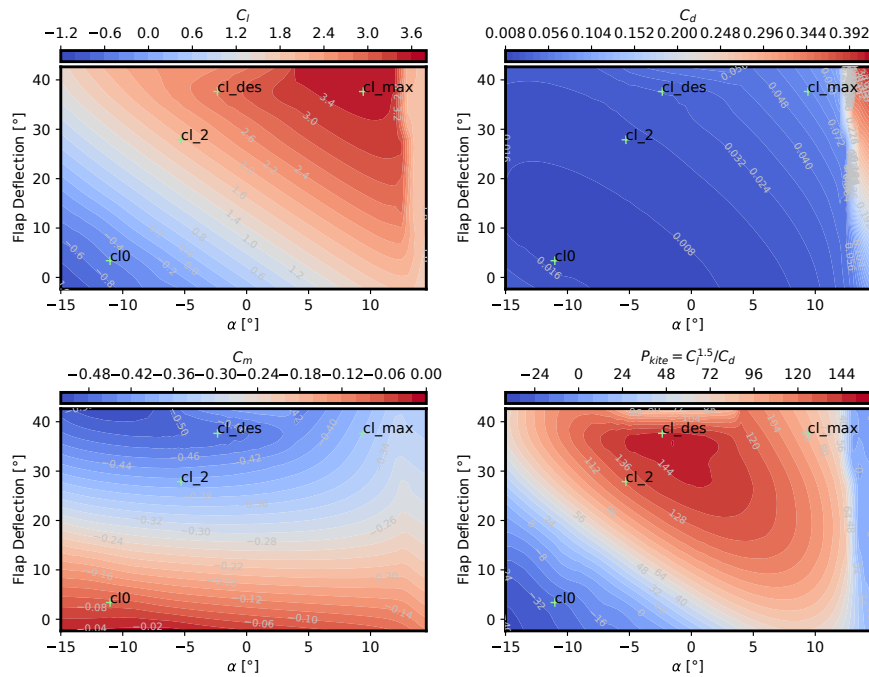
4.3.2 Aerodynamic performance

Figure 13: Flap deflection study for DA90 at $Re = 3 \times 10^6$.

In figure 13 and 14, the aerodynamic performance of *DA90* and the reference aerofoil from Porta Ko et al.[10] is plotted. The data was obtained using *ADflow* and the SA turbulence model. The green crosses mark specific operating points such as **cl_des** which is the nominal desing operating point.

Difference to Reported Values by Porta Ko et al. When comparing the data in figure 14 to the reference plots in Porta Ko et al.,[10] it can be seen that the values for lift and moment are similar. But the predicted drag from *ADflow* is approximately 15% higher. Since we are comparing two different turbulence models (SST vs. SA), this discrepancy should be acceptable.

Lift Coefficient The maximum usable lift coefficient (**cl_des**) needs to be as high as possible as it directly influences the pulling force on the tether. The higher this force is, the more electrical power may be generated. At this operating point, *DA90* shows an increase form 2.5 to 2.8 counts.

Once the tether is fully extended, the plane needs to fly back down as fast as possible to retreat it again. The time this maneuver takes is dictated by the lowest usable lift coefficient (**cl0**). As this was a constraint, both values are similar. But it has to be noted that **DA90**'s usable region extends well below this operating point. Thus the constraint could probably be lifted up to $C_l = 0$ which would allow the optimizer to increase C_l at **cl_des** even more.

Kite Performance. When comparing P_{kite}, it is important to look at the region between **cl_des** and **cl_2**. The first one represents the nominal operating point and the second one a lower lift coefficient for higher wind speeds. The aerofoil from Porta Ko et al.[10] varies in that region between 131 and 108 counts. Whereas *DA90* moves from 147 to 128 counts with a peek of 150 in between.

Moment coefficient. When looking at C_m in the whole operating range, it can be seen that *DA90* has significantly higher values all around. The peek at any operating point increases from −0.31 to −0.47. As a matter of fact, we did not add any upper limit for C_m, letting the optimiser maximize the second element's lift and thus move the centre of pressure backwards. It is well known, however, that a high aerodynamic moment may become impractical as it

may force the designers to increase strength and stiffness of wing structure and all connections. For this reason C_m is normally constrained in a realistic design process.

Summary. In general, *DA90* shows outstanding aerodynamic characteristics except pitching moment. Due to the limited time in preparing this exercise for the present paper, C_m was not constrained. Based on the practical experience gained, a better solution can be found with consideration of C_m in further optimisation iterations.
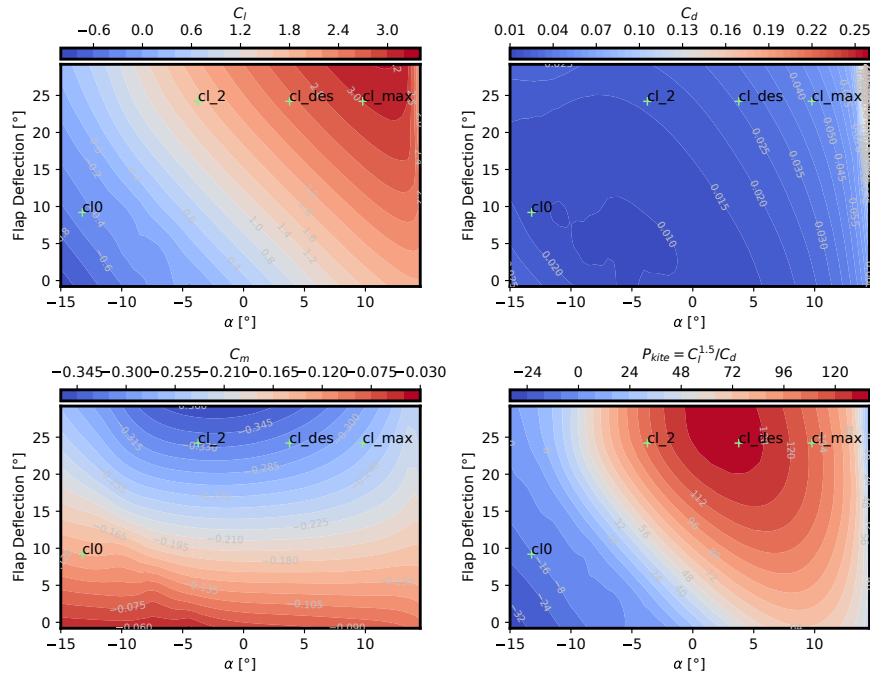

Figure 14: Flap deflection study for Porta Ko et al. at $Re = 3 \times 10^6$.

5. Conclusions

This paper gives an overview of numerical optimisation activities conducted at ZHAW for single- and multi-element aerofoils using gradient-based tools. We chose three test cases derived from real-life problems in wind turbine and UAV applications. The three case studies represent three aerofoil design and optimisation developments for industrial projects. In the presented studies, we used two optimisation chains to improve the aerofoil performance. The first tool suite includes NASA's OpenMDAO framework, ADflow and other open-source packages developed by the MDO Lab. The second optimisation process was driven by Ansys Fluent. In addition, we combined the gradient-based method with statistical models based on Design of Experiments and the conventional inverse method for aerofoil optimisation. To support the numerical optimisation work, we conducted several wind tunnel campaigns. The aim of the experiments is not only to establish a good correlation between the measured and calculated data, but also to collect experience which may help to improve the numerical optimisation approach.

Both gradient-based tools associated with the adjont method proved to be powerful and robust for the presented applications. The practical challenges encountered in the daily operations of our industry partners were properly considered during the aerofoil design phase. For the single-element case, we provided a solution under considerations of surface roughness, which has a significant impact on performance of thick aerofoils at low Reynolds numbers. In the multi-element cases, the good performance was achieved both at design points and in a relatively broad operation area (off-design points) within the flight envelope.

The open-source tool chain ADflow and the commercial Ansys products exhibit differences in user handling, due to their distinct development philosophies. The MACH framework has been primarily developed for aeronautical applications, while the Ansys tools are designed to address a wide range of engineering disciplines and provide users with various problem-solving options. These differences reflect in the geometric parametrisation step, for example when specifying traditional aerofoil and wing characteristics or defining constraints for flap motion in a high-lift system. Consequently, ADflow excels in efficiently exploring optimisation solutions starting from a rough baseline. On the other hand, Ansys fluent is better suited for local refinement of an existing design or the cases dealing with complex

geometry. The GEKO turbulence model has been implemented in Ansys CFD. It allows to include turbulence model parameters, specially tailored to the specific flow field, among the design variables in the adjoint-based optimisation process. For industrial projects, we highly recommend to customise the general workflow to align with the specific requirements of the project.

Last but not least, we would like to emphasise that the conventional inverse method using velocity or pressure distribution, in conjunction with panel code, RANS solver, or even adjoint solver, continues to hold significant value in solving industrial problems. Despite the advancements in computational techniques, it is important to maintain a commitment to "old-fashioned" methodologies that incorporate fundamental physics and well-established engineering practices.

6. Acknowledgments

References

[1] ANSYS, Inc. *Ansys Fluent User's Guide*. ANSYS, Inc.

[2] W. Kenneth Bullivant. Tests of the NACA 0025 and 0035 airfoils in the full-scale wind tunnel. Technical Report NACA-TR-708, National Advisory Committee for Aeronautics, January 1941.

[3] Oleg Chernukhin and David W. Zingg. Multimodality and global optimization in aerodynamic design. *AIAA Journal*, 51(6):1342–1354, June 2013.

[4] Antonello Cherubini, Andrea Papini, Rocco Vertechy, and Marco Fontana. Airborne wind energy systems: A review of the technologies. *Renewable and Sustainable Energy Reviews*, 51:1461–1476, 2015.

[5] Gaetan K. W. Kenway, Charles A. Mader, Ping He, and Joaquim R.R.A. Martins. Effective adjoint approaches for computational fluid dynamics. *Progress in Aerospace Sciences*, 110:100542, 2015.

[6] Emil K. Kruse, Niels N. Sorensen, and Christian Bak. A two-dimensional quantitative parametric investigation of simplified surface imperfections on the aerodynamic characteristics of a NACA 633-418 airfoil. *Wind Energy*, 24(4):305–408, 2021.

[7] Charles A. Mader, Gaetan K. W. Kenway, Anil Yildirim, and Joaquim R.R.A. Martins. ADflow: An open-source computational fluid dynamic solver for aerodynamic and multidisciplinary optimization. *Journal of Aerospace Information Systems*, 17(9):508–527, Sep 2020.

[8] F. R. Menter. Two-equation eddy-viscosity turbulence models for engineering applications. *AIAA Journal*, 32(8):1598–1605, 1994.

[9] F. R. Menter, R. Lechner, and A. Mayushenko. Best Practice: Generalized $k - \omega$ (GEKO) Two-Equation Turbulence Modeling in Ansys CFD. Technical report, ANSYS Germany GmbH, NTS, St. Petersburg, Russia, 2021.

[10] Agusti Porta Ko, Sture Smidt, Roland Schmehl, and Manoj Mandru. Optimisation of a multi-element airfoil for a fixed-wing airborne wind energy system. *Energies*, 16(8):3521, Apr 2023.

[11] D. Ragni, C. Simao Ferreira, and G. Correale. Experimental investigation of an optimized airfoil for vertical-axis wind turbines. *Wind Energy*, 18:1629–1643, 2015.

[12] M. Righi, D. Anderegg, L. Manfriani, M. Ammann, C. Oram, A. Yildirim, J. R. Martins, and O. Coretti. Optimisation of symmetrical aerofoils for a vertical axis wind turbine. In *Proceedings of the AIAA Aviation 2022 Forum*, Chicago, IL, June 2022. AIAA 2022-3384.

[13] H. Schlichting and K. Gersten. *Grenzschicht-Theorie*. Springer Berlin, xxiii edition, 2006.

[14] Ney Secco, Gaetan K. W. Kenway, Ping He, Charles A. Mader, and Joaquim R. R. A. Martins. Efficient mesh generation and deformation for aerodynamic shape optimization. *AIAA Journal*, 59(3), June 2020.

[15] P. R. Spalart and S. R. Allmaras. A one-equation turbulence model for aerodynamic flows. In *Proceedings of the AIAA 30th Aerospace Sciences Meeing and Exhibit*, Reno, IL, USA, 6-9 January 1992.